Ceramics International 51 (2025) 50941–50950

Contents lists available at ScienceDirect

Ceramics International

journal homepage: www.elsevier.com/locate/ceramint

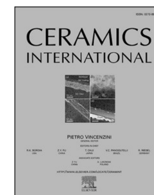

Ferroelectric $Hf_{0.5}Zr_{0.5}O_2$ thin films on TiN/Si substrates grown by pulsed laser deposition at CMOS-compatible temperatures

C.F. Chirila [a,*], G.A. Boni [a], D.G. Popescu [a], C.M. Istrate [a], M.A. Husanu [a], L.D. Filip [a], C. Besleaga [a], L. Pintilie [a], A. Dimoulas [a,b]

[a] National Institute of Materials Physics, Atomistilor 405A, Magurele, Romania

[b] Institute of Nanoscience and Nanotechnology, National Center for Scientific Research DEMOKRITOS, Attiki, Neapoleos 27 and Patriarchou Gigoriou Str., 15341, Athens, Greece

ARTICLE INFO

Keywords:
CMOS-Compatible
Ferroelectric HZO phase
Oxygen vacancies
Pulsed laser deposition

ABSTRACT

Doped hafnium oxide is of great interest for its compatibility with silicon-based semiconductor technology and potential for nanoscale ferroelectric applications. However, controlling thin-film crystallinity and stabilizing metastable ferroelectric phases remain challenging. This study investigates 7.5 nm-thick $Hf_{0.5}Zr_{0.5}O_2$ (HZO) thin films deposited on Si/TiN substrates using low-temperature pulsed laser deposition (PLD), followed by rapid thermal annealing (RTA). Notably, the as-grown film at 400 °C already exhibits a stabilized orthorhombic phase and strong ferroelectricity, achieving a remnant polarization (P_r) of 12.5 μC/cm^2 at an applied field of 1.9 MV/cm. In contrast, RTA at 600 °C induces a transition to the monoclinic phase and reduces overall crystallinity. Compared to atomic layer and chemical solution deposition methods, PLD enables superior crystallinity and phase control. Our results highlight that low-temperature PLD facilitates orthorhombic phase stabilization via kinetic control of oxygen vacancies, eliminating the need for high-temperature annealing or wake-up cycling to achieve robust ferroelectric behavior.

1. Introduction

HfO_2-based thin films exhibit a range of advantageous characteristics that render them highly attractive for both academic research and industrial applications [1–5] These materials are particularly notable for their compatibility with silicon technology, facile chemical synthesis, and lead-free composition, addressing both technological and environmental considerations [6,7]. A defining characteristic of doped HfO_2 thin films is the emergence of ferroelectricity down to the nanometer scale [8–10]. Surprisingly, the robust ferroelectricity could be maintained even the thickness of HfO_2 was scaled down to 1 nm, as evidenced using piezoresponse microscopy and second harmonic generation measurements [11]. This behavior is in stark contrast with conventional perovskite-based ferroelectric materials, where ferroelectricity typically diminishes with decreasing thickness, except in epitaxially grown films under well-defined conditions [12,13]. The ability of doped HfO_2 films to sustain and even improve ferroelectricity at ultra-thin dimensions positions them as promising candidates for integration into next-generation electronic devices for low power electronics [2]. Numerous methods have been employed for the fabrication of HfO_2-based thin films, including chemical solution deposition [14], reactive sputtering [15], molecular beam epitaxy [16], atomic layer deposition (ALD) [10], and pulsed laser deposition (PLD) [17–19]. Among these, ALD has emerged as the most widely adopted technique due to its capability to achieve precise thickness control and high uniformity across large areas. However, the performance of ALD-derived HfO_2 films is highly dependent on post-annealing processes conducted ex-situ, which play a critical role in determining the material's structural and ferroelectric properties. Remnant polarization values in the range of 10–40 μC/cm^2 can be achieved when the orthorhombic $Pca2_1$ phase (o-phase) is stabilized. According to the literature, this phase in HfO_2-based films can be formed at temperatures between 400 °C and 800 °C. Films grown at lower temperatures require a post-deposition rapid thermal annealing (RTA) step to induce ferroelectricity, whereas those that directly crystallize into the $Pca2_1$ phase typically necessitate substrate temperatures above 700 °C or the use of different buffer or seed layers, as observed in the growth of HfO_2 thin films by PLD on STO or Si substrates [5,19–21]. Mitigation of the wakeup effect and improving

* Corresponding author.
E-mail address: dragoi@infim.ro (C.F. Chirila).

https://doi.org/10.1016/j.ceramint.2025.08.321
Received 22 May 2025; Received in revised form 24 July 2025; Accepted 21 August 2025
Available online 22 August 2025
0272-8842/© 2025 Elsevier Ltd and Techna Group S.r.l. All rights are reserved, including those for text and data mining, AI training, and similar technologies.

endurance are critically dependent on the incorporation of specific dopants, such as Si [22,23], La [17], and Y [11], which modulate the crystallization process and energetically favor the polar orthorhombic structure. Among the various studied compositions, a 1:1 mixture of $Hf_{0.5}Zr_{0.5}O_2$ (HZO) has been identified as offering the broadest process window for the stabilization of the ferroelectric phase. The results reported here presents a novel approach for the direct stabilization of the o-phase in a 1:1 mixture of HZO thin films on silicon/titanium nitride (Si/TiN) substrates via pulsed laser deposition (PLD). The aim of this study is to demonstrate that PLD can directly stabilize the orthorhombic ferroelectric phase in $Hf_{0.5}Zr_{0.5}O_2$ thin films at low temperature (400 °C), without post-deposition annealing, and to correlate this behavior with structural and theoretical insights. The direct formation of the ferroelectric o-phase at such a moderate temperature constitutes a substantial advancement in the processing of HZO thin films, enabling the simplification of the fabrication workflow. The elimination of RTA not only reduces energy consumption but also mitigates effects such as impurity retention and interfacial degradation, which are prevalent in high-temperature annealing processes. The decrease in processing temperature is especially crucial for semiconductor manufacturing, since it conforms to the strict thermal budgets of CMOS-compatible technologies. Our findings demonstrate that PLD at 400 °C enables the stabilization of the o-phase through kinetic regulation of oxygen vacancy formation, thereby eliminating the necessity for high-temperature post-deposition annealing. We found that annealing of the as-grown samples at elevated temperatures in an N_2 flow facilitates the generation of a higher amount of oxygen vacancies, which influences the structural and electrical properties and contributes to an increase in leakage current, with a significant impact on the ferroelectric polarization.

2. Experimental section

TiN films were grown using radio-frequency magnetron sputtering (RF-MS) with a customized AJA Phase II J system on 10–30 Ω cm p-type silicon substrates, oriented along 111 (Topsil GlobalWafers A/S) crystallographic planes. The depositions were performed at room temperature without intentional heating, although the substrate temperature rose to approximately 50 °C due to plasma bombardment. A metallic titanium target was sputtered in a reactive atmosphere comprising 50 sccm argon (Ar) and 3 sccm nitrogen (N_2) at a working pressure of 0.5 Pa. During deposition, the substrate was rotated and biased at −70 V, while a power of 275 W was applied to the target.

HZO layer was grown using PLD with a KrF excimer laser ($\lambda = 248$ nm) supplied by Surface GmbH. Prior to deposition, the substrate was maintained on preheated to 550 °C under high vacuum, 1×10^{-4} Pa for 1 h. Preheating substrates under high vacuum conditions is a common practice in epitaxial layer deposition to remove contaminants and improve film quality [24]. After this pretreatment, the substrate was cooled at a controlled rate of 10 °C/min to 400 °C. During this phase, a controlled oxygen atmosphere of 10 Pa was introduced into the deposition chamber. The HZO thin film, approximately 7.5 nm thick, was grown by ablating a high-purity HZO target using a laser frequency of 2 Hz, fluence of 1.1 J/cm^2, and energy of 39 mJ at the target surface. The target-to-substrate distance was maintained at 55 mm. Following the deposition, the oxygen atmosphere in the chamber was adjusted to 20 Pa, and the sample was cooled to room temperature without a ramping program. Three samples were prepared, with one analyzed in the as-grown state and the others subjected to RTA under different conditions. The RTA annealing parameters were as follows: 600 °C for 20 s and 450 °C for 400 s, both performed in an N_2 atmosphere at 0.5 atm. The annealing process was conducted using a custom-built tubular RTA furnace equipped with a system of four 150 W halogen lamps emitting in the infrared spectrum. These lamps were symmetrically positioned above and below the sample in semi-embedded steel enclosures. Temperature control was achieved using JUMO Quantrol LC300 to ensure precise thermal profiles. The annealing program and the furnace setup are schematically represented in Fig. 1. These processes were used to evaluate the effects of RTA on the structural and electrical properties of the HZO thin films.

Information about global structure, symmetry and phase-mixing was derived from Grazing Incidence X-ray diffraction (XRD) with a Cu Kα source (Anton Paar - XRDynamic 500 system). The scans were conducted over an angular range of $2\theta = 25$–$35°$, with a step size of 0.04°, and time per step of 17 s.

The transmission electron microscopy (TEM) investigations have been performed on an analytical electron microscope JEM-ARM 200F operated at 200 kV. TEM specimens were prepared through mechanical polishing to a thickness of approximately 30 μm, followed by ion milling using a Gatan PIPS system operated at 4 kV accelerating voltage and a 7° incidence angle. A final low-voltage ion milling step was employed to minimize the amorphous surface layer surrounding the specimen. The microstructural analysis of the HZO thin films was performed using two complementary approaches, namely: HR-TEM images, which provide information on the lattice plane spacing, and FFT patterns derived from the HR-TEM images.

X-ray photoelectron spectroscopy measurements (XPS) were conducted in a dedicated Kratos AXIS Ultra DLD chamber, equipped with a monochromatized X-ray source having a spot size of 0.7 mm, using Al $K_{\alpha}1$ (1486.74 eV) radiation and a hemispherical analyzer with a reference intensity of over 50.000 counts per second (cps) and spectral resolution of 0.6 eV. The operating power was 144 W (12 kV × 12 mA). The spectra were recorded with 160 eV pass energy for surveys and 40 eV pass energy for high-resolution measurements. Hybrid lens mode and slot aperture were used. Partial charge compensation is achieved with a neutralizer flood gun (filament current of 1.8 A, charge balance of 2.7 V, filament bias of 1.0 V). The base pressure in the analysis chamber was kept below 1×10^{-7} Pa and the energies were calibrated to the C 1s spectrum (284.60 ± 0.01 eV). The core levels are fitted with Voigt lines and their corresponding backgrounds associated to the inelastic scattering of photoelectrons [25].

Theoretical calculations have been performed using the Quantum Espresso (QE) plane wave package [26,27] and local density approximation (LDA) for the exchange and correlation functional. Norm-conserving pseudopotentials from the Pseudo Dojo library were used.

Hysteresis measurements of polarization and current–voltage loops are carried out with a TF Analyzer 2000 ferroelectric tester. Electrical measurements were conducted using a capacitor plate geometry, Pt top electrodes were deposited via sputtering, employing a TEM grid as a shadow mask to define the electrode geometry. The resulting circular electrodes had a diameter of 20 μm, corresponding to an area of approximately 314 μm^2, with a thickness of 20 nm. The connection between the electrodes and measurement units was established using a LakeShore CPX-VF probe station.

3. Results and discussion

The current HZO thin films present a mixed m- and o-phase, which is consistent with previous reports [28]. Fig. S1 show the fitting grazing-angle incidence x-ray diffraction (GIXRD) (incidence angle $\omega = 0.5°$) patterns of the RTA 450 °C, RTA 600 °C and as grown by PLD samples. The RTA-treated sample at 600 °C tend to form more m-phase, while the other two films show a more suppressed m-phase contribution. The film RTA 450 °C and as grown by PLD show similar trends. The Bragg diffraction signatures at ~30.2° is attributed to polar o-phase. However, the slight shift in the Bragg angle from the reference, ~30.4°, might indicate that the HZO films are strained in the compressive in-plane state [29]. The agreement between the peak positions in XRD and the lattice features observed on HR-TEM, Figs. 2 and 3 supports the identification of the orthorhombic phase.

TEM analysis of the as-grown sample reveals that the HZO layer has a

Ceramics International 51 (2025) 50941–50950

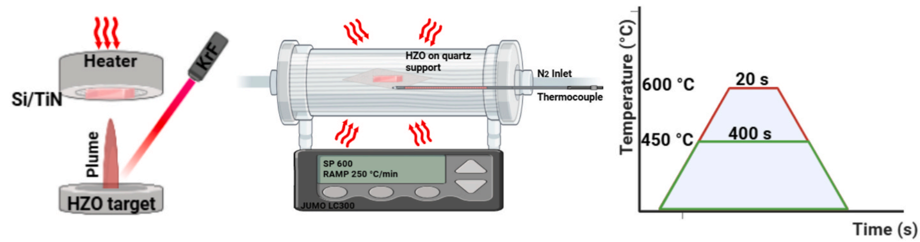

Fig. 1. Schematic representation of deposition and post-processing process. using PLD and RTA.

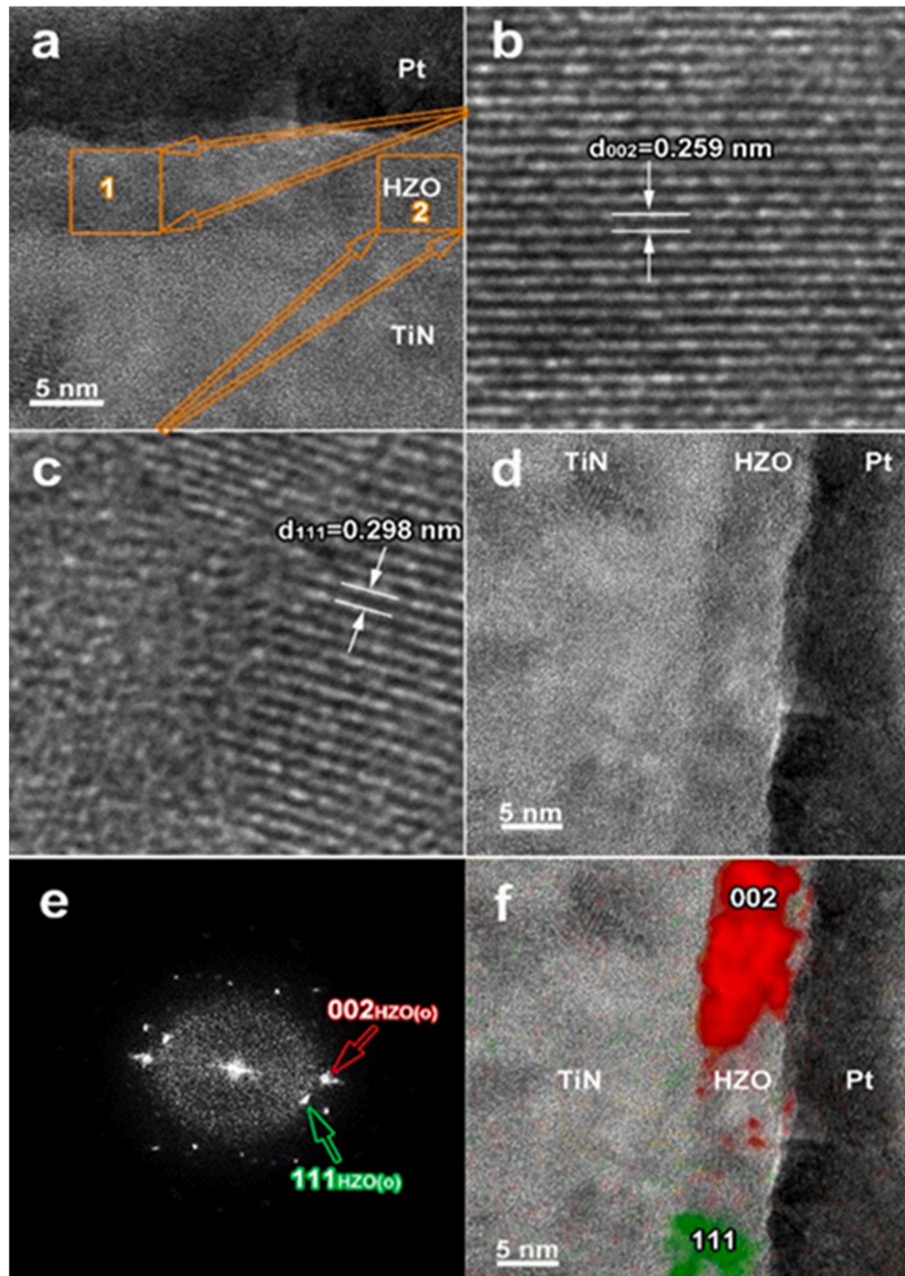

Fig. 2. (a) Cross-sectional HR-TEM image of the sample, (b–c) magnified views of the lattice fringes of HZO extracted from the two orange squares; the measured lattice fringes were assigned to the $(002)_{HZO(o)}$ and $(111)_{HZO(o)}$ lattice planes of the o-phase of HZO, (d) Same cross-sectional HR-TEM image of the sample as it was recorded in the microscope, (e) FFT pattern corresponding to the HR-TEM image, (d–f) Bragg filtered image obtained by filtering $(002)_{HZO(o)}$ and $(111)_{HZO(o)}$ peaks from the FFT pattern which clearly show the spatial distribution of the HZO(o) crystallites. (For interpretation of the references to color in this figure legend, the reader is referred to the Web version of this article.)

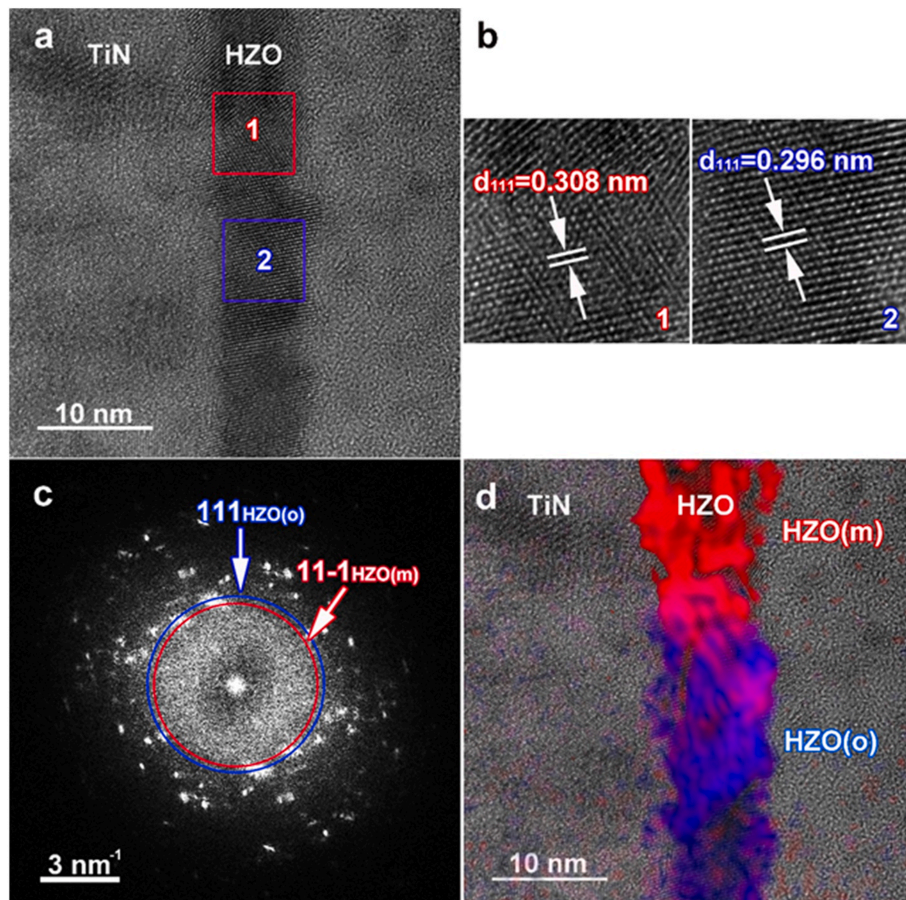

Fig. 3. (a) HR-TEM image of a HZO/TiN region, (b) detail extracted from the HR-TEM image of a zone axis oriented HZO(m) and HZO(o), (c) FFT pattern corresponding to the HR-TEM image, (d) IFFT image embedded in the HR-TEM image to show the spatial distribution of the o-phase and the spatial distribution of the m-phase of the HZO thin film, across the analyzed area.

thickness of approximately ~7.5 nm whereas the thickness of the TiN electrode is 35 nm. Fig. S2 display the SAED pattern which correspond to the TEM image recorded from an area which contains both the HZO layer and TiN electrode and also the Si substrate, on the as-grown sample. A set of intense peaks emerging from the central diffraction peak can be observed and assigned to the Si substrate according to the subscripts shown in Fig. S2. The ring diffraction pattern can be assigned to the TiN electrode confirming its polycrystalline structure. Owing to the polycrystalline structure of TiN, the SAED analysis does not reveal a clear crystallographic orientation relationship between the HZO and the TiN electrode. The Si substrate is oriented along [1–23] zone axis with the [111] direction parallel to the out-of-plane direction. To gain deeper insight into the microstructure of the HZO, HR-TEM experiments were conducted.

Due to the unfavorable geometry between the thin film thickness (7.5 nm) and the projected diameter of the smallest available selected-area aperture no favorably oriented HZO grains were captured. As a result, no intensity peaks associated with the HZO can be observed in the SAED pattern. In the case of HZO, the o-phase, responsible for the ferroelectric behavior, can be discerned from the m-phase, which is much more stable at room temperature, by analyzing the {111} lattice planes spacing. In the case of the o-phase the $\{111\}_o$ family lattice planes are spaced at 0.2958 nm, while for the m-phase we have a splitting in two family of planes, namely $\{11\text{-}1\}_m$ and $\{111\}_m$, spaced at 0.314 nm and 0.282 nm, respectively.

Fig. 2a presents a high-magnification TEM image revealing the interfaces between Pt/HZO and HZO/TiN. Fig. 2b and c displays two distinct regions from the HZO, extracted from the two orange squares in the HR-TEM image, both favorably oriented along a main crystallographic axis. Measurements of the lattice fringe distances yielded two distinct values: 0.259 nm and 0.298 nm. These values correspond to the $(002)_o$ and $(111)_o$ lattice planes of the HZO o-phase, respectively, consistent with the reported lattice parameters (a = 0.50 nm, b = 0.503 nm, and c = 0.522 nm) [30]. The FFT pattern from Fig. 2e corresponds to the HR-TEM image shown in Fig. 2d. The main FFT peaks were measured indexed and assigned to the $(002)_o$ and $(111)_o$ planes of the o-phase of HZO. The obtained values are consistent with the ones measured in the HR-TEM micrographs from Fig. 2b and c. To visually emphasize the spatial distribution of the analyzed HZO areas, FFT filtering of the HR-TEM micrograph was performed. In Fig. 2f, the mixed-colored image highlights the spatial distribution of specific lattice planes, with red representing the intensity map corresponding to the $(002)_o$ peaks and green corresponding to the $(111)_o$ peaks. This representation clearly reveals the granular microstructure of the HZO. Although the previous HR-TEM analysis confirmed the o-phase of the HZO, the possible presence of minor phases, such as the m-phase, cannot be completely ruled out, due to the local character of the TEM technique. Considering this, another region of film, shown in the HR-TEM micrograph in Fig. S3, was analyzed. By measuring the distance between the lattice fringes in Fig. S3b, a spacing of 0.314 nm was obtained, which can be assigned to the $(11\text{-}1)_m$ lattice planes of the m-phase HZO. This finding strongly suggests the presence of a minor m-phase in the HZO. Overall, these results are in excellent agreement with the XRD measurements, which also indicate a major o-phase with a minor m-phase in the as-grown sample.

TEM analysis of the RTA-treated sample 600 °C reveals that the HZO

layer has a thickness of approximately 7.5 nm, while the TiN electrode layer maintains a thickness of 35 nm, consistent with its as-grown state. This confirms that the TiN layer was unaffected by the annealing process. Fig. S4(right) display the SAED pattern which correspond to the TEM image recorded from an area encompassing both the HZO layer and TiN electrode and also the Si substrate. A set of intense diffraction peaks emerging from the central diffraction peak can be observed and assigned to the Si substrate, while weaker peaks can be assigned to the m- and o-phase. The ring shaped diffraction pattern can be assigned to the TiN electrode which demonstrate the polycrystalline structure. Due to the polycrystalline structure of TiN, from the SAED analysis no crystallographic orientation relationship between the HZO thin film and the TiN electrode can be derived. The Si substrate is oriented along [−112] zone axis with the [111] direction parallel to the out-of-plane direction. Unlike the previous sample, one can notice the presence of some weaker intensity peaks which were indexed and assigned to the HZO. The presence of the two weaker peaks in the SAED pattern, associated with the m- and o phase of the HZO, suggests that the metastable orthorhombic-to-monoclinic transition occurs more frequently, after the annealing treatment, than in the previous sample where the orthorhombic structure is significantly more stable. To determine the possible crystalline phases of the HZO, the same HR-TEM and FFT analysis as for the previous sample was performed.

Due to the granular nature of the HZO, regions where the film is favorably oriented along a principal crystallographic axis were analyzed. An example of such a region is presented in the HR-TEM image in Fig. 3a, where a neat and sharp interface between the TiN electrode and the HZO can be observed. Fig. 3b displays HR-TEM images showing two favorably oriented HZO grains extracted from the blue and red squares, labeled as regions 1 and 2, respectively. Measurements of the lattice fringes in these regions yielded two distinct values: 0.308 nm for region 1 and 0.296 nm for region 2. The distinction between the m- and o-phases was previously discussed in the above HR-TEM section. From the measurements performed on both HR-TEM images, the lattice fringes in region 1 can be assigned to the $(11\text{-}1)_m$ lattice planes of the m-phase, while those in region 2 correspond to the $(111)_o$ lattice planes of the o-phase. Fig. 3c presents the FFT pattern corresponding to the HR-TEM image in Fig. 3a, in which two circles are drawn. The red circle has a radius corresponding to 0.308 nm in real space and can be attributed to the $(11\text{-}1)_m$ lattice planes, while the blue circle corresponds to 0.296 nm and is associated with the $(111)_o$ lattice planes. This analysis confirms the polycrystalline nature of the HZO, consisting of a mixture of m and o-phases. The Fourier-filtered image in Fig. 3d highlights the spatial distribution of specific lattice planes, with red representing the intensity map corresponding to the $(11\text{-}1)_m$ peaks and blue representing the $(111)_o$ peaks. This visualization further reveals the granular and polycrystalline microstructure of the HZO thin film. Unlike the as-grown sample, the HR-TEM analysis clearly indicates here a higher net contribution of the m-phase, as was revealed also by XRD.

Fig. 4 displays O *1s* (a,d,g), Zr *3d* (b,e,h) and Hf *4f* (c,f,i) spectra for

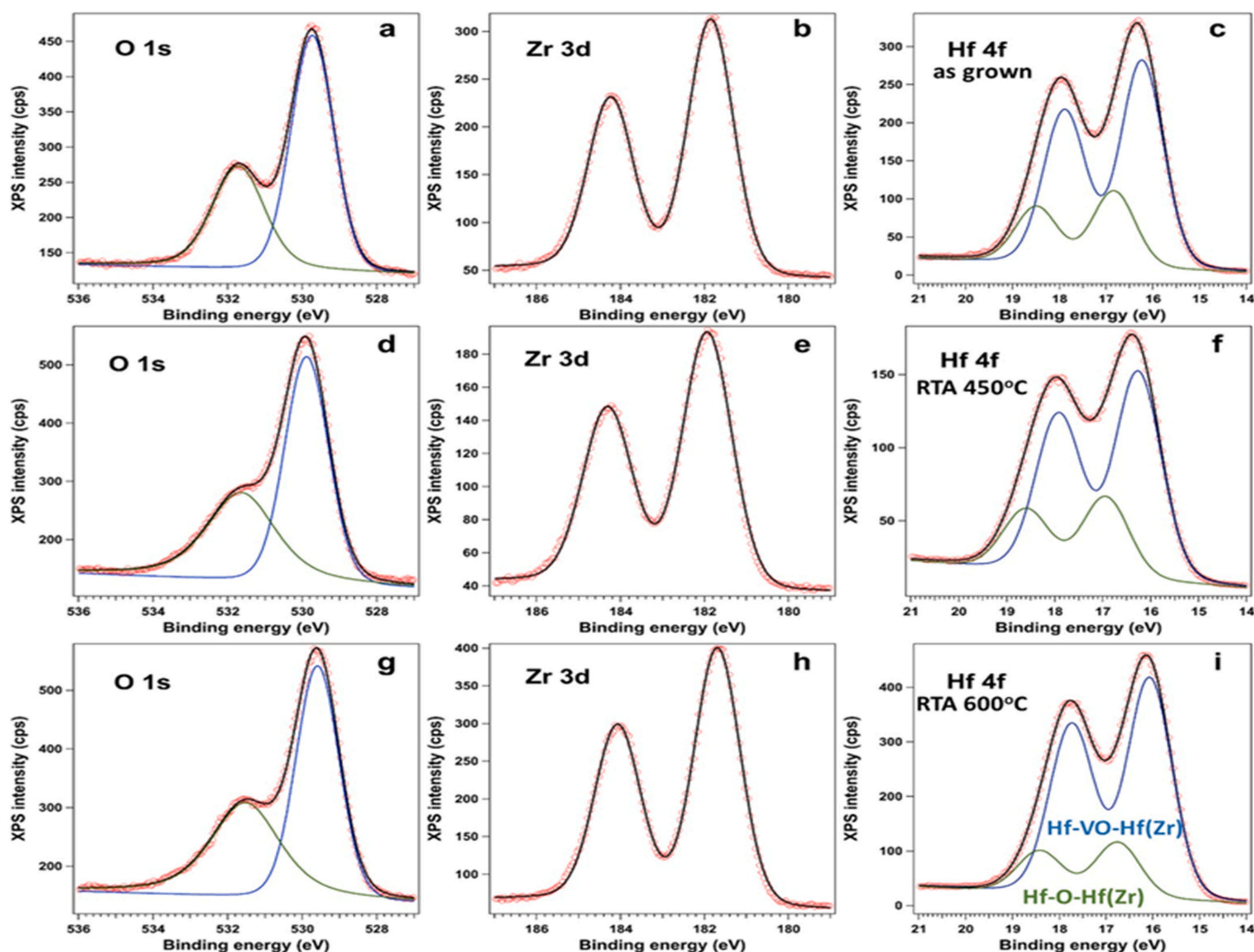

Fig. 4. (a–c) O 1s, Zr 3d and Hf 4f XPS spectra of as-grown HZO, (d–f) HZO after RTA at 450°C and after RTA at 600°C.

respectively as-grown HZO, HZO after RTA at 450°C and HZO after RTA at 600°C. O *1s* spectra are featured by two components corresponding to O in HZO at ~529.7 eV and a second component at 531.6 eV corresponding to contamination species. Zr *3d* fits well with a single component with the $3d^{3/2}$ maxima at 181.7 eV. Hf features two valence states: Hf^{4+} in the stoichiometric HZO environment and reduced due to creation of oxygen vacancies (VO) to Hf^{3+}. The Hf:Zr is in all samples close to the 1:1 ratio from the PLD target.

Assuming that Hf and Zr are isotropically distributed within HZO, with each Hf atom ideally bonded by four oxygen atoms, and that only single vacancies occur around Hf and Zr atoms, we can deduce the amount of VOs from the ratio of the Hf^{3+} and Hf^{4+} components, scaled by a factor of four. The values are given in Table 1.

Remarkably, upon RTA at 600°C, the ratio between Hf in the oxygen deficient environment and in the ideal environment Hf-O-Hf(Zr) increases, indicating the significant development of oxygen vacancies during the treatment at elevated temperatures. This finding is further corroborated by the electrical measurements, where an increase of the leakage current takes place, leakage current that prevents the ferroelectric switching from being highlighted for this sample. Noteworthy, recent studies [31–33] aimed to disclose the presence of oxygen vacancies as a distinct peak in the O *1s* spectrum. However, this fundamentally overlooks that the signal in photoemission comes from the existing species, not from the missing ones. On the other hand, the species remaining in the material and previously bonded to the oxygen will experience significant chemical shifts due to the altered environment caused by the loss of oxygen.

Numerical DFT calculations were used to investigate the connection between the VO concentration and polarization in HZO. To this effect, 1, 2 and 4 VO's have been introduced in two HZO geometries: unit-cell and super-cell, in order to obtain a relevant range of vacancy concentration. In the unit-cell geometry only 1 VO has been considered and it creates the highest concentration of 0.125. With the super-cell geometry concentrations of 0.015625, 0.03125 and 0.0625 can be obtained. For each vacancy case there are several positions where the vacancies can be placed, either in relation to polar or symmetric part of the unit-cell/super-cell or within the same section (for the multiple vacancies cases). All the considered cases have been summarized in Table S1 in the supplemental material. The atomic coordinates are that of o-phase HfO_2 space group. We used one 1x1x1 unit cell with 12 atoms and $2 \times 2 \times 2$ supercells with 96 atoms. The total energy and force per atom was converged to less than 10^{-3} eV/atom. Zr atoms were stoichiometrically inserted to account for the experimental value Hf:Zr = 1:1. Relaxation of the unit cell and of the internal coordinates were performed on an automatically generated, uniform $4 \times 4 \times 4$ Monkhorst–Pack k-mesh. For Berry phase calculations self-consistent followed by non-self-consistent calculations were performed with $8 \times 8 \times 8$ k-meshes. All computations were performed with 80 Ry kinetic-energy cut-off for the plane waves.

Fig. S6 summarizes the polarization values in Table S1 for each vacancy concentration and vacancy placement. The necessary polarization branch corrections are shown in Table S1 together with the formation energies per vacancy in each case. While the overall polarization values are in the expected range and in agreement with similar studies in the literature [34,35] there is no definitive conclusion that can be drawn with regards to the placement of the vacancies. The VO formation energy column shows that all the structures are essentially unstable structures with no clear preference to one particular arrangement. This result is in line with the experimental conclusions that the HZO ferroectric phaze is unstable and each unstable VO placement can be found in a real HZO sample. For this reason a more reasonable approach is to plot the average polarization for each VO placement corresponding to each concentration case (see Fig. 5). It is revealed that an optimum concentration exists for the VO's that can maximize the spontaneous polarization in the sample. Further increases of the concentration lead to a lower polarization and possibly to a destabilization of the polar phase.

Table 1
Oxygen deficiency in HZO after thermal treatment.

HZO	As-prepared	RTA 450°C	RTA 600°C
%VO	9.16 %	9.02 %	10.02 %

Another aspect that must be underlined is the apparent discrepancy between the experimental polarization value and the calculated one. As it can be observed from the structural investigations, the ferroelectric phase of HZO is embedded in a non-ferroelectric matrix, this strongly increases the difference between the saturated polarization and remnant one by approximately 50 %. This result is consistent with other results in the literature [34,35] and the results in this study. The calculated polarization is the saturated polarization which explains the higher value. The remnant polarization that is obtained after the domains have relaxed throughout the sample cannot be accessed by DFT methods.

These DFT results correlate well with the observed trend in polarization amplitude, supporting the hypothesis that an optimal vacancy concentration promotes ferroelectric stabilization, while excessive vacancy content leads to phase destabilization.

To perform the electrical characterization, full polarization–voltage (P–V) loops were first recorded and are presented in Fig. 6. These measurements qualitatively illustrate the polarization switching behavior of the HZO thin films. However, it should be noted that the P–V loops exhibit a certain degree of distortion—particularly broadening—due to leakage currents present in the structure. As a result, the loops cannot be used as a fully quantitative measure of remnant polarization. For this reason, the ferroelectric switchable behavior of HZO thin films was characterized using polarization versus voltage (P-V) loops, measured via the Positive-Up Negative-Down (PUND) method [36]. Bistable switching and well-defined hysteresis loops were observed at room temperature and a frequency of 1 kHz, for both the as-grown sample and the sample annealed at 450 °C, Fig. 7.

PUND is a method used to characterize the switching behavior and polarization of ferroelectric materials, isolating remnant polarization from other contributions such as non-switching polarization and leakage current. It involves applying a sequence of voltage pulses: P (a positive pulse that switches polarization to the positive state), U (a positive pulse that does not switch polarization but measures parasitic contributions), N (a negative pulse that switches polarization to the negative state), and D (a negative pulse that does not switch polarization but measures parasitic contributions). By subtracting the non-switching contributions (U or D) from the corresponding switching pulses (P or N), the switching polarization and remnant polarization can be accurately determined. The results clearly indicate significant differences between the current, which includes the switching contribution (evidenced by the peaks), and the non-switching contribution. These measurements provide clear

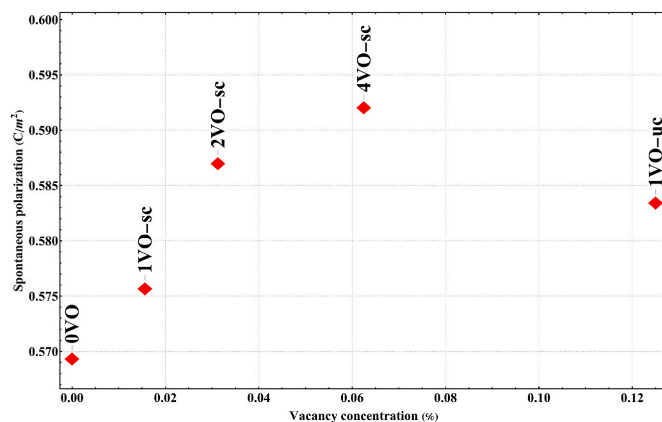

Fig. 5. The average polarization for each VO placement corresponding to each concentration case.

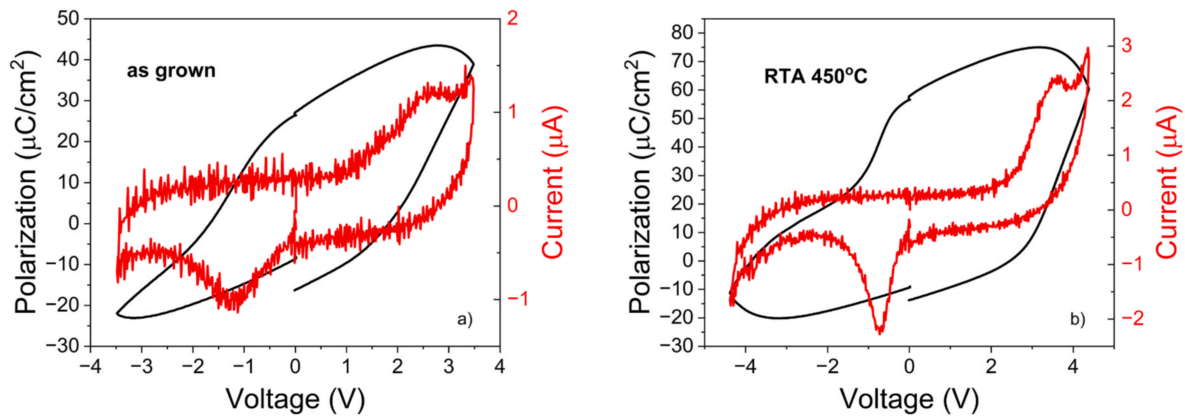

Fig. 6. (a–b) Full polarization-voltage loops for as-grown and RTA 450 °C.

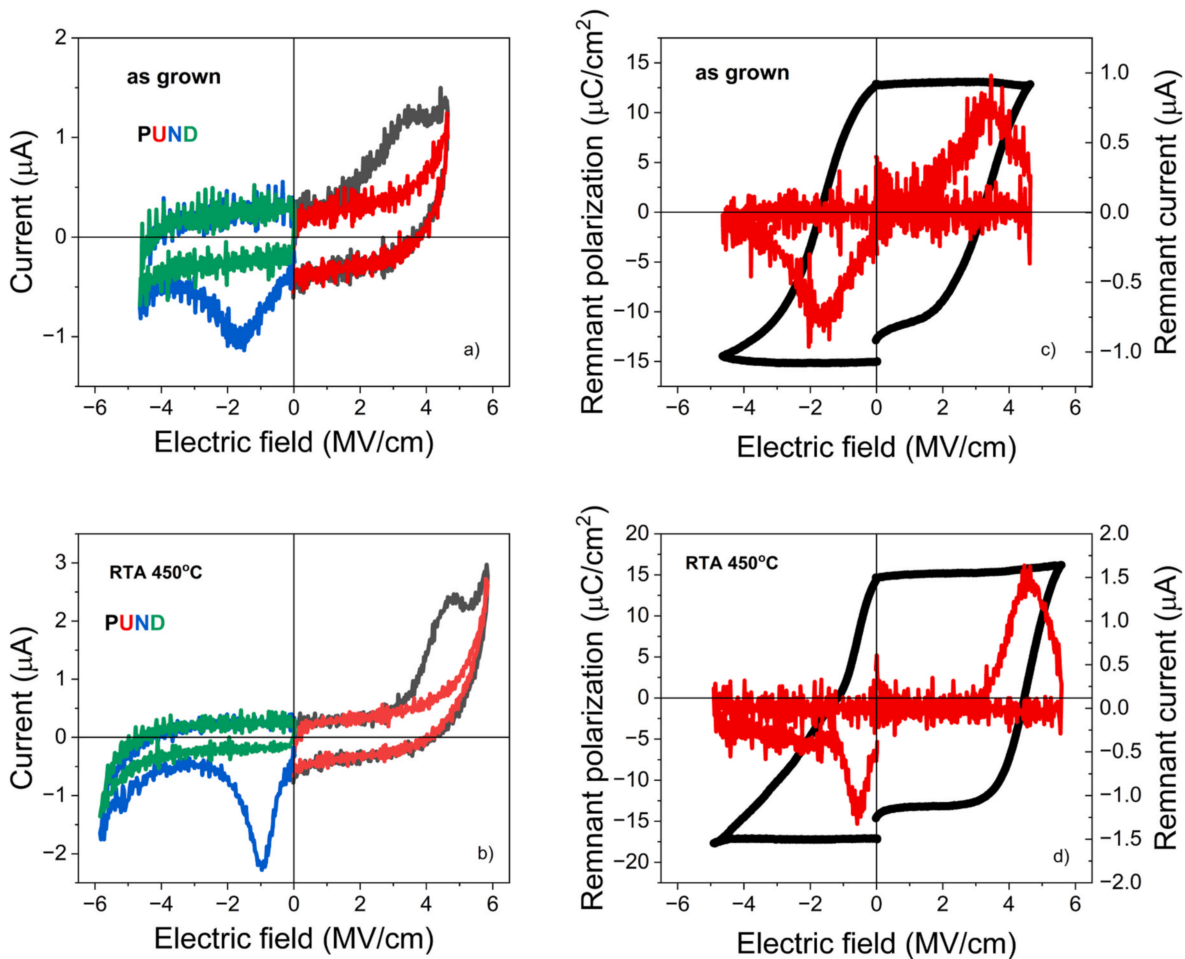

Fig. 7. (a–b) The current-voltage characteristics determined by PUND pulse sequence; (c–d) and remnant polarization, for as-grown and RTA 450 °C.

evidence of polarization switching and confirm the ferroelectric nature of the samples. For both samples, the non-switching characteristics exhibit, in addition to the dielectric displacement current, a substantial contribution from leakage, especially at high voltages. Subtracting these non-switching contributions yields the remnant current, as shown in Fig. 7a and b. By integrating the current-voltage characteristics, the remnant polarization is obtained (represented by the black loops in Fig. 7c and d. For the as-grown sample, the remnant polarization is 12.5 $\mu C/cm^2$, and the coercive voltage is 1.9 MV/cm, with an imprint towards positive voltages of approximately 0.5 V. For the annealed sample, the remnant polarization is about 15 $\mu C/cm^2$, the coercive voltage is 2.2 MV/cm, and the imprint towards positive voltages is 1.27 V. In this case, the full reversal of polarization for positive voltage is not completed within the applied voltage range. At higher voltages, HZO breakdown occurs due to large electric fields and significant leakage. A remnant polarization of 12.5 $\mu C/cm^2$ on as-grown sample, representing a significant improvement compared to previously reported values for hafnia-based oxides grown on silicon substrates by PLD [19,28]. The robust ferroelectric behavior in the PLD-grown sample without the need for any wakeup training was obtained. This suggests intrinsic

ferroelectricity obtained by control achieved during deposition. To mitigate the risk of dielectric breakdown, the applied voltage on the HZO thin films was incrementally increased in 1 V steps. It is important to emphasize that this procedure was implemented as a preventative measure and should not be interpreted as an occurrence of the wake-up effect. The electrical performance metrics typically associated with device-level benchmarks (such as endurance and retention) are not addressed in this study, primarily due to contact degradation during cycling and the limited number of testable capacitors. Nevertheless, this limitation does not diminish the significance of the findings. The results clearly demonstrate that direct stabilization of the ferroelectric orthorhombic phase can be achieved at CMOS-compatible temperatures (400 °C) without requiring post-deposition annealing or wake-up conditioning.

The dielectric constant (ε_r) was estimated from the slope of the charge density (D) versus voltage (V) curve, as it is directly related to the material's permittivity. The displacement field D and the electric field E are connected through the relation: $D = \varepsilon_0 \varepsilon_r E$ [37], where ε_0 is the permittivity of free space. Considering that the electric field is given by $E = V/d$, where d is the film thickness, the dielectric constant can be extracted from the slope of the D-V curve as: $\varepsilon_r = \left(\frac{dD}{dV}\right) \cdot \left(\frac{d}{\varepsilon_0}\right)$. This method was employed to determine the dielectric constant of HZO/-TiN/Si samples using the charge–voltage curves obtained for the second pulse in the PUND measurement. For this pulse, polarization reversal does not contribute to the dielectric constant of these structures, ensuring that the extracted values correspond to the intrinsic dielectric response. The slope was determined at low voltages, where leakage currents have no significant contribution. The analysis is presented in Fig. 8. These results, showing a dielectric constant of 38.8 for the as-grown sample and 24.14 for the RTA 450 °C sample, are consistent with previous studies, where variations in dielectric constant are attributed to the ratio between different crystalline phases [38–40].

Although our first-principles calculations predict a significant increase of the polarization for oxygen off-stoichiometry x = 0.125, this behavior cannot be evidenced on the HZO films subjected to an RTA processes at 600 °C due to the leakage current, Fig. S7. Leakage is also the possible source of consistently smaller values of the measured polarizations compared to the calculated values. This behavior is more likely related to the presence of the mobile defects, particularly oxygen vacancies, that significantly influence the ferroelectric properties of HZO thin films [41,42]. These vacancies can migrate and accumulate at grain boundaries or interfaces, forming localized electric fields that impede domain wall motion, thereby hindering polarization switching [43]. First-principles calculations have provided insights into the influence of oxygen vacancies in monoclinic HfO_2 by altering the local electronic structure and potentially stabilizing non-ferroelectric phases [42,44]. Additionally, studies on ferroelectric materials like $BaTiO_3$ indicate that oxygen vacancies can cluster, leading to the formation of charged domain walls, which modify the material's ferroelectric behavior [45]. Our DFT-deduced increase of the polarization in HZO, assisted by the oxygen vacancies, although not suitable for its electric functionality due to the accompanying large leakage, could be highly relevant for the stabilization of ferroelectric topological states such as ferroelectric skyrmions [46] at the interface between the ferroelectric, o-phase and the insulating monoclinic one. An optimal concentration of such vacancies can aid in stabilizing the desired ferroelectric phase, while excessive vacancies may lead to the formation of non-ferroelectric phases, degrading the material's performance [41]. We associate our findings with the fact that the high-energy environment inherent to PLD often leads to the creation of oxygen vacancies within thin films. For instance, in the deposition of $SrFeO_3$, Bi_2FeCrO_6, or $PbZrTiO_3$ thin films, PLD under standard conditions typically results in oxygen-deficient films, requiring additional oxidation processes to achieve the desired stoichiometry [12,47,48]. Therefore, by carefully selecting deposition parameters and post-deposition annealing conditions, it is possible to achieve an optimal concentration of oxygen vacancies for stabilizing the desired ferroelectric phase and enhancing the overall performance of HZO thin films.

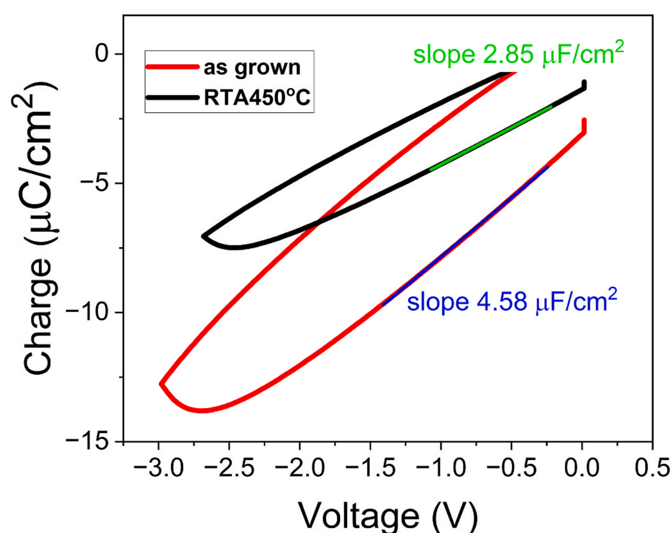

Fig. 8. Charge density (D) versus voltage (V) characteristics.

4. Conclusions

This study demonstrates a composition–structure–property guided approach to stabilize the ferroelectric o-phase in $Hf_{0.5}Zr_{0.5}O_2$ thin films through controlled pulsed laser deposition at CMOS-compatible temperatures. By investigating HZO films deposited at a substrate temperature of 400 °C under a low oxygen partial pressure of 10 Pa, along with the effects of post-deposition thermal processing on identically prepared samples, we establish a direct correlation between processing conditions and the stabilization of metastable phases in fluorite-structured ferroelectrics.

Key findings reveal that.

1. PLD growth at 400 °C enables direct formation of the ferroelectric o-phase without requiring post-deposition annealing, achieving a remnant polarization of 12.5 μC/cm^2;
2. The stable ferroelectric response without prior wakeup training confirms the intrinsic nature of the PLD-grown films;
3. Rapid thermal annealing at 600 °C promotes transformation to the m-phase while increasing oxygen vacancy concentration to 10.02 %, as verified by XPS;
4. An optimal oxygen vacancy concentration around 9 % was identified for maintaining both phase stability and ferroelectric performance.
5. Significant increase of the polarization is predicted in first-principles calculations upon the appearance of oxygen vacancies.

These results provide fundamental insights into defect-mediated phase stabilization in HZO thin films and establish quantitative composition-structure-property relationships. The demonstrated control over kinetic pathways through deposition parameters offers a framework for designing metastable ferroelectric phases in other fluorite-structured materials systems. Furthermore, the CMOS-compatible thermal budget of this approach presents significant advantages for back-end-of-line integration in semiconductor manufacturing. For low-power or energy-efficient applications, the as-grown sample is preferable due to its lower coercive field and smaller imprint, even if it has slightly lower polarization. While this study successfully demonstrates the direct stabilization of the ferroelectric orthorhombic phase in HZO thin films grown by low-temperature PLD, several limitations remain. Notably, temperature-dependent electrical characterization and long-

term endurance measurements could not be performed due to contact degradation and limited capacitor reliability. Despite these constraints, the structural and functional results provide clear evidence of intrinsic ferroelectric behavior and offer a solid foundation for future work. Continued efforts will focus on improving electrode stability, enabling thermal and cycling robustness, and ultimately bridging the gap between materials-level discovery and reliable device-level implementation.

CRediT authorship contribution statement

C.F. Chirila: Writing – review & editing, Writing – original draft, Methodology, Conceptualization. **G.A. Boni:** Writing – original draft, Validation, Investigation, Data curation. **D.G. Popescu:** Writing – original draft, Validation, Methodology, Investigation. **C.M. Istrate:** Writing – original draft, Visualization, Validation, Investigation. **M.A. Husanu:** Writing – original draft, Validation, Software, Investigation. **L. D. Filip:** Writing – original draft, Validation, Software. **C. Besleaga:** Writing – original draft, Validation, Investigation. **L. Pintilie:** Writing – review & editing, Writing – original draft, Validation, Supervision, Resources. **A. Dimoulas:** Writing – review & editing, Writing – original draft, Validation, Resources, Project administration.

Data availability statement

The data that support the finding of the present study are available from the corresponding author upon reasonable request.

Declaration of competing interest

The authors have no conflicts to disclose.

Acknowledgments

The authors acknowledge financial support through the PNRR project 760239/December 28, 2023, funded by the Romanian Ministry of Research, Innovation and Digitization through the National Recovery and Resilience Plan, and Core Program, component project PN23080202, funded by Romanian Ministry of Research, Innovation and Digitization.

Appendix A. Supplementary data

Supplementary data to this article can be found online at https://doi.org/10.1016/j.ceramint.2025.08.321.

References

[1] J. Müller, P. Polakowski, S. Mueller, T. Mikolajick, Ferroelectric hafnium oxide based materials and devices: Assessment of current status and future prospects, ECS J. Solid State Sci. Technol. 4 (2015) N30, https://doi.org/10.1149/2.0081505jss.

[2] R. Ramesh, S. Salahuddin, S. Datta, C.H. Diaz, D.E. Nikonov, I.A. Young, D. Ham, M.-F. Chang, W.-S. Khwa, A.S. Lele, C. Binek, Y.-L. Huang, Y.-C. Sun, Y.-H. Chu, B. Prasad, M. Hoffmann, J.-M. Hu, Z. Yao, L. Bellaiche, P. Wu, J. Cai, J. Appenzeller, S. Datta, K.Y. Camsari, J. Kwon, J.A.C. Incorvia, I. Asselberghs, F. Ciubotaru, S. Couet, C. Adelmann, Y. Zheng, A.M. Lindenberg, P.G. Evans, P. Ercius, I.P. Radu, Roadmap on low-power electronics, APL Mater. 12 (2024) 099201, https://doi.org/10.1063/5.0184774.

[3] A.I. Khan, A. Keshavarzi, S. Datta, The future of ferroelectric field-effect transistor technology, Nat Electron 3 (2020) 588–597, https://doi.org/10.1038/s41928-020-00492-7.

[4] J.Y. Park, D.-H. Choe, D.H. Lee, G.T. Yu, K. Yang, S.H. Kim, G.H. Park, S.-G. Nam, H.J. Lee, S. Jo, B.J. Kuh, D. Ha, Y. Kim, J. Heo, M.H. Park, Revival of ferroelectric memories based on emerging fluorite-structured ferroelectrics, Adv. Mater. 35 (2023) 2204904, https://doi.org/10.1002/adma.202204904.

[5] M.H. Park, Y.H. Lee, C.S. Hwang, Understanding ferroelectric phase formation in doped HfO2 thin films based on classical nucleation theory, Nanoscale 11 (2019) 19477–19487, https://doi.org/10.1039/C9NR05768D.

[6] M. Hoffmann, U. Schroeder, T. Schenk, T. Shimizu, H. Funakubo, O. Sakata, D. Pohl, M. Drescher, C. Adelmann, R. Materlik, A. Kersch, T. Mikolajick, Stabilizing the ferroelectric phase in doped hafnium oxide, J. Appl. Phys. 118 (2015) 072006, https://doi.org/10.1063/1.4927805.

[7] H. Lu, D.-J. Kim, H. Aramberri, M. Holzer, P. Buragohain, S. Dutta, U. Schroeder, V. Deshpande, J. Íñiguez, A. Gruverman, C. Dubourdieu, Electrically induced cancellation and inversion of piezoelectricity in ferroelectric Hf0.5Zr0.5O2, Nat. Commun. 15 (2024) 860, https://doi.org/10.1038/s41467-024-44690-9.

[8] T. Song, R. Bachelet, G. Saint-Girons, N. Dix, I. Fina, F. Sánchez, Thickness effect on the ferroelectric properties of La-doped HfO2 epitaxial films down to 4.5 nm, J. Mater. Chem. C 9 (2021) 12224–12230, https://doi.org/10.1039/D1TC02512K.

[9] B. Noheda, P. Nukala, M. Acuautla, Lessons from hafnium dioxide-based ferroelectrics, Nat. Mater. 22 (2023) 562–569, https://doi.org/10.1038/s41563-023-01507-2.

[10] A. Sünbül, D. Lehninger, R. Hoffmann, R. Olivo, A. Prabhu, F. Schöne, K. Kühnel, M. Döllgast, N. Haufe, L. Roy, T. Kämpfe, K. Seidel, L.M. Eng, Impact of ferroelectric layer thickness on reliability of back-end-of-line-compatible hafnium Zirconium oxide films, Adv. Eng. Mater. 25 (2023) 2201124, https://doi.org/10.1002/adem.202201124.

[11] S.S. Cheema, N. Shanker, C.-H. Hsu, A. Datar, J. Bae, D. Kwon, S. Salahuddin, One nanometer HfO2-based ferroelectric Tunnel Junctions on silicon, Advanced Electronic Materials 8 (2022) 2100499, https://doi.org/10.1002/aelm.202100499.

[12] L. Pintilie, C. Ghica, C.M. Teodorescu, I. Pintilie, C. Chirila, I. Pasuk, L. Trupina, L. Hrib, A.G. Boni, N. Georgiana Apostol, L.E. Abramiuc, R. Negrea, M. Stefan, D. Ghica, Polarization induced self-doping in epitaxial Pb(Zr0.20Ti0.80)O3 thin films, Sci. Rep. 5 (2015) 14974, https://doi.org/10.1038/srep14974.

[13] M.F. Sarott, U. Bucheli, A. Lochmann, M. Fiebig, M. Trassin, Controlling the polarization in ferroelectric PZT films via the epitaxial growth conditions, Adv. Funct. Mater. 33 (2023) 2214849, https://doi.org/10.1002/adfm.202214849.

[14] M. Badillo, S. Taleb, T. Mokabber, J. Rieck, R. Castanedo, G. Torres, B. Noheda, M. Acuautla, Low-toxicity chemical solution deposition of ferroelectric Ca:HfO2, J. Mater. Chem. C 11 (2023) 1119–1133, https://doi.org/10.1039/D2TC04182K.

[15] Y.H. Lee, H.J. Kim, T. Moon, K.D. Kim, S.D. Hyun, H.W. Park, Y.B. Lee, M.H. Park, C.S. Hwang, Preparation and characterization of ferroelectric Hf0.5Zr0.5O2 thin films grown by reactive sputtering, Nanotechnology 28 (2017) 305703, https://doi.org/10.1088/1361-6528/aa7624.

[16] C. Zacharaki, S. Chaitoglou, N. Siannas, P. Tsipas, A. Dimoulas, Hf0.5Zr0.5O2-Based germanium ferroelectric p-FETs for nonvolatile memory applications, ACS Appl. Electron. Mater. 4 (2022) 2815–2821, https://doi.org/10.1021/acsaelm.2c00324.

[17] T. Song, R. Bachelet, G. Saint-Girons, R. Solanas, I. Fina, F. Sánchez, Epitaxial ferroelectric La-doped Hf0.5Zr0.5O2 thin films, ACS Appl. Electron. Mater. 2 (2020) 3221–3232, https://doi.org/10.1021/acsaelm.0c00560.

[18] A. Silva, I. Fina, F. Sánchez, J.P.B. Silva, L. Marques, V. Lenzi, Unraveling the ferroelectric switching mechanisms in ferroelectric pure and La doped HfO2 epitaxial thin films, Materials Today Physics 34 (2023) 101064, https://doi.org/10.1016/j.mtphys.2023.101064.

[19] P. Nukala, J. Antoja-Lleonart, Y. Wei, L. Yedra, B. Dkhil, B. Noheda, Direct epitaxial growth of polar (1 – x)HfO2–(x)ZrO2 Ultrathin films on silicon, ACS Appl. Electron. Mater. 1 (2019) 2585–2593, https://doi.org/10.1021/acsaelm.9b00585.

[20] T. Song, R. Bachelet, G. Saint-Girons, I. Fina, F. Sánchez, Ferroelectric Hf0.5Zr0.5O2 films with improved endurance obtained through low temperature epitaxial growth on seed layers, Nanoscale 15 (2023) 5293–5299, https://doi.org/10.1039/D2NR05935E.

[21] J. Lyu, I. Fina, J. Fontcuberta, F. Sánchez, Epitaxial integration on Si(001) of ferroelectric Hf0.5Zr0.5O2 capacitors with high retention and endurance, ACS Appl. Mater. Interfaces 11 (2019) 6224–6229, https://doi.org/10.1021/acsami.8b18762.

[22] T. Li, M. Ye, Z. Sun, N. Zhang, W. Zhang, S. Inguva, C. Xie, L. Chen, Y. Wang, S. Ke, H. Huang, Origin of ferroelectricity in epitaxial Si-doped HfO2 films, ACS Appl. Mater. Interfaces 11 (2019) 4139–4144, https://doi.org/10.1021/acsami.8b19558.

[23] E. Yurchuk, J. Müller, S. Knebel, J. Sundqvist, A.P. Graham, T. Melde, U. Schröder, T. Mikolajick, Impact of layer thickness on the ferroelectric behaviour of silicon doped hafnium oxide thin films, Thin Solid Films 533 (2013) 88–92, https://doi.org/10.1016/j.tsf.2012.11.125.

[24] Y.-P. Lan, The influence of the preheating temperature of the (?2 0 1) ?-Ga2O3 substrates on c-plane GaN epitaxial growth, Coatings 11 (2021) 824, https://doi.org/10.3390/coatings11070824.

[25] C.M. Teodorescu, J.M. Esteva, R.C. Karnatak, A. El Afif, An approximation of the Voigt I profile for the fitting of experimental X-ray absorption data, Nucl. Instrum. Methods Phys. Res. Sect. A Accel. Spectrom. Detect. Assoc. Equip. 345 (1994) 141–147, https://doi.org/10.1016/0168-9002(94)90983-0.

[26] P. Giannozzi, S. Baroni, N. Bonini, M. Calandra, R. Car, C. Cavazzoni, D. Ceresoli, G.L. Chiarotti, M. Cococcioni, I. Dabo, A. Dal Corso, S. de Gironcoli, S. Fabris, G. Fratesi, R. Gebauer, U. Gerstmann, C. Gougoussis, A. Kokalj, M. Lazzeri, L. Martin-Samos, N. Marzari, F. Mauri, R. Mazzarello, S. Paolini, A. Pasquarello, L. Paulatto, C. Sbraccia, S. Scandolo, G. Sclauzero, A.P. Seitsonen, A. Smogunov, P. Umari, R.M. Wentzcovitch, Quantum ESPRESSO: a modular and open-source software project for quantum simulations of materials, J. Phys. Condens. Matter 21 (2009) 395502, https://doi.org/10.1088/0953-8984/21/39/395502.

[27] P. Giannozzi, O. Andreussi, T. Brumme, O. Bunau, M. Buongiorno Nardelli, M. Calandra, R. Car, C. Cavazzoni, D. Ceresoli, M. Cococcioni, N. Colonna, I. Carnimeo, A. Dal Corso, S. de Gironcoli, P. Delugas, R.A. DiStasio, A. Ferretti, A. Floris, G. Fratesi, G. Fugallo, R. Gebauer, U. Gerstmann, F. Giustino, T. Gorni, J. Jia, M. Kawamura, H.-Y. Ko, A. Kokalj, E. Küçükbenli, M. Lazzeri, M. Marsili, N. Marzari, F. Mauri, N.L. Nguyen, H.-V. Nguyen, A. Otero-de-la-Roza, L. Paulatto,

S. Poncé, D. Rocca, R. Sabatini, B. Santra, M. Schlipf, A.P. Seitsonen, A. Smogunov, I. Timrov, T. Thonhauser, P. Umari, N. Vast, X. Wu, S. Baroni, Advanced capabilities for materials modelling with Quantum ESPRESSO, J. Phys. Condens. Matter 29 (2017) 465901, https://doi.org/10.1088/1361-648X/aa8f79.

[28] H.W. Cho, P. Pujar, M. Choi, S. Kang, S. Hong, J. Park, S. Baek, Y. Kim, J. Lee, S. Kim, Direct growth of orthorhombic Hf0.5Zr0.5O2 thin films for hysteresis-free MoS2 negative capacitance field-effect transistors, Npj 2D Mater Appl 5 (2021) 1–8, https://doi.org/10.1038/s41699-021-00229-w.

[29] J. Lyu, I. Fina, R. Solanas, J. Fontcuberta, F. Sánchez, Growth window of ferroelectric epitaxial Hf0.5Zr0.5O2 thin films, ACS Appl. Electron. Mater. 1 (2019) 220–228, https://doi.org/10.1021/acsaelm.8b00065.

[30] https://next-gen.materialsproject.org/materials/mp-685097?formula=HfO2), (n. d.).

[31] J. Dai, Y. Zhu, H.A. Tahini, Q. Lin, Y. Chen, D. Guan, C. Zhou, Z. Hu, H.-J. Lin, T.-S. Chan, C.-T. Chen, S.C. Smith, H. Wang, W. Zhou, Z. Shao, Single-phase perovskite oxide with super-exchange induced atomic-scale synergistic active centers enables ultrafast hydrogen evolution, Nat. Commun. 11 (2020) 5657, https://doi.org/10.1038/s41467-020-19433-1.

[32] Y. Wang, R. Yang, Y. Ding, B. Zhang, H. Li, B. Bai, M. Li, Y. Cui, J. Xiao, Z.-S. Wu, Unraveling oxygen vacancy site mechanism of Rh-doped RuO2 catalyst for long-lasting acidic water oxidation, Nat. Commun. 14 (2023) 1412, https://doi.org/10.1038/s41467-023-37008-8.

[33] Q. Li, S. Wang, Z. Li, X. Hu, Y. Liu, J. Yu, Y. Yang, T. Wang, J. Meng, Q. Sun, D. W. Zhang, L. Chen, High-performance ferroelectric field-effect transistors with ultra-thin indium tin oxide channels for flexible and transparent electronics, Nat. Commun. 15 (2024) 2686, https://doi.org/10.1038/s41467-024-46878-5.

[34] S. Clima, D.J. Wouters, C. Adelmann, T. Schenk, U. Schroeder, M. Jurczak, G. Pourtois, Identification of the ferroelectric switching process and dopant-dependent switching properties in orthorhombic HfO2: a first principles insight, Appl. Phys. Lett. 104 (2014) 092906, https://doi.org/10.1063/1.4867975.

[35] W. Wei, X. Ma, J. Wu, F. Wang, X. Zhan, Y. Li, J. Chen, Spontaneous polarization enhancement in ferroelectric Hf0.5Zr0.5O2 using atomic oxygen defects engineering: an ab initio study, Appl. Phys. Lett. 115 (2019) 092905, https://doi.org/10.1063/1.5115293.

[36] K.M. Rabe, M. Dawber, C. Lichtensteiger, C.H. Ahn, J.-M. Triscone, Modern physics of ferroelectrics:essential background, in: Physics of Ferroelectrics: A Modern Perspective, Springer, Berlin, Heidelberg, 2007, pp. 1–30, https://doi.org/10.1007/978-3-540-34591-6_1.

[37] Front matter, in: K.C. Kao (Ed.), Dielectric Phenomena in Solids, Academic Press, San Diego, 2004, p. iii, https://doi.org/10.1016/B978-0-12-396561-5.50020-7.

[38] A. Kashir, M.G. Farahani, H. Hwang, Towards an ideal high-κ HfO2–ZrO2-based dielectric, Nanoscale 13 (2021) 13631–13640, https://doi.org/10.1039/D1NR02272E.

[39] S.S. Cheema, N. Shanker, L.-C. Wang, C.-H. Hsu, S.-L. Hsu, Y.-H. Liao, M. San Jose, J. Gomez, W. Chakraborty, W. Li, J.-H. Bae, S.K. Volkman, D. Kwon, Y. Rho, G. Pinelli, R. Rastogi, D. Pipitone, C. Stull, M. Cook, B. Tyrrell, V.A. Stoica, Z. Zhang, J.W. Freeland, C.J. Tassone, A. Mehta, G. Saheli, D. Thompson, D.I. Suh, W.-T. Koo, K.-J. Nam, D.J. Jung, W.-B. Song, C.-H. Lin, S. Nam, J. Heo, N. Parihar, C.P. Grigoropoulos, P. Shafer, P. Fay, R. Ramesh, S. Mahapatra, J. Ciston, S. Datta, M. Mohamed, C. Hu, S. Salahuddin, Ultrathin ferroic HfO2–ZrO2 superlattice gate stack for advanced transistors, Nature 604 (2022) 65–71, https://doi.org/10.1038/s41586-022-04425-6.

[40] A. Kashir, H. Hwang, A CMOS-compatible morphotropic phase boundary, Nanotechnology 32 (2021) 445706, https://doi.org/10.1088/1361-6528/ac1716.

[41] A.V. Dmitriyeva, S.S. Zarubin, A.S. Konashuk, S.A. Kasatikov, V.V. Popov, A. V. Zenkevich, Controlling ferroelectric properties in Y-doped HfO2 thin films by precise introduction of oxygen vacancies, J. Appl. Phys. 133 (2023) 054103, https://doi.org/10.1063/5.0131893.

[42] K. McKenna, A. Shluger, The interaction of oxygen vacancies with grain boundaries in monoclinic HfO2, Appl. Phys. Lett. 95 (2009) 222111, https://doi.org/10.1063/1.3271184.

[43] J. Lee, K. Yang, J.Y. Kwon, J.E. Kim, D.I. Han, D.H. Lee, J.H. Yoon, M.H. Park, Role of oxygen vacancies in ferroelectric or resistive switching hafnium oxide, Nano Convergence 10 (2023) 55, https://doi.org/10.1186/s40580-023-00403-4.

[44] K.Z. Rushchanskii, S. Blügel, M. Ležaić, Ordering of oxygen vacancies and related ferroelectric properties in ${\mathrm{HfO}}_{2\ensuremath{-}\ensuremath {\delta, Phys. Rev. Lett. 127 (2021) 087602, https://doi.org/10.1103/PhysRevLett.127.087602.

[45] U. Petralanda, M. Kruse, H. Simons, T. Olsen, Oxygen vacancies nucleate charged domain walls in ferroelectrics, Phys. Rev. Lett. 127 (2021) 117601, https://doi.org/10.1103/PhysRevLett.127.117601.

[46] Y. Nahas, S. Prokhorenko, L. Louis, Z. Gui, I. Kornev, L. Bellaiche, Discovery of stable skyrmionic state in ferroelectric nanocomposites, Nat. Commun. 6 (2015) 8542, https://doi.org/10.1038/ncomms9542.

[47] E. Enriquez, A. Chen, Z. Harrell, X. Lü, P. Dowden, N. Koskelo, M. Janoschek, C. Chen, Q. Jia, Oxygen vacancy-driven evolution of structural and electrical properties in SrFeO3−δ thin films and a method of stabilization, Appl. Phys. Lett. 109 (2016) 141906, https://doi.org/10.1063/1.4964384.

[48] X. Henning, K. Alhada-Lahbabi, D. Deleruyelle, B. Gautier, L. Schlur, T. Fix, S. Colis, A. Dinia, M.V. Rastei, Oxygen vacancy effects on polarization switching of ferroelectric ${\mathrm{Bi}}_{2}{\mathrm{FeCrO}}_{6}$ thin films, Phys. Rev. Mater. 8 (2024) 054416, https://doi.org/10.1103/PhysRevMaterials.8.054416.